Mechanical Systems and Signal Processing 211 (2024) 111113

Contents lists available at ScienceDirect

Mechanical Systems and Signal Processing

journal homepage: www.elsevier.com/locate/ymssp

# Frictional phenomena within a quasi zero stiffness vibration device

A.D. Shaw [a,*], G. Gatti [b], P.J.P. Gonçalves [c], B. Tang [d], M.J. Brennan [c]

[a] Faculty of Science and Engineering, Swansea University, Swansea, UK
[b] Department of Mechanical, Energy and Management Engineering, University of Calabria, Rende, Italy
[c] Department of Mechanical Engineering, Faculty of Engineering, UNESP, Bauru, Brazil
[d] School of Energy and Power Engineering, Dalian University of Technology, Dalian, China

ARTICLE INFO

Communicated by H. Ouyang

Dataset link: https://doi.org/10.5281/zenodo.10340200

*Keywords:*
Quasi Zero Stiffness
Isolation
Friction
Isola
Nonlinear vibration

ABSTRACT

Quasi Zero Stiffness (QZS) devices have received widespread interest due to their potential applications in vibration isolation and as nonlinear energy sinks. However, as the stiffness is driven towards zero, the response becomes dominated by the effects of damping and friction. This places a strong emphasis on accurate modelling of these effects if realistic results are to be achieved. This work analyses and experimentally demonstrates the complex responses that can occur in a frictional QZS device, including isolated response regions and non-sinusoidal responses. This is done using a simple device recently developed by the authors that allows accurate adjustment of the nonlinear force–displacement curve. Furthermore, high frequency disturbances on the frictional system are shown to introduce a damping effect on the low frequency behaviour, and an equivalent linear damping coefficient is derived.

## 1. Introduction

Quasi Zero Stiffness (QZS) devices exploit nonlinearity to achieve a near zero dynamic stiffness, whilst maintaining the ability to withstand static loads without excessive displacements [1]. There have been many implementations of QZS devices, including but not limited to buckled beams [2], electromagnetic effects [3,4], 3D compliant mechanisms [5–7], X-shaped mechanical linkages [8,9], constant force mechanisms [10] and even origami based approaches [7,11–13]. They have been deployed as vibration isolators, nonlinear energy sinks [14–18] and energy harvesters [19,20]. An interesting recent development is including mass within the isolator, creating nonlinear inertial effects to further shape the resulting response [21]. Furthermore, many authors are considering QZS approaches to achieving low frequency resonances within mechanical metamaterials with a recent intriguing example exploiting shape memory allows to achieve temperature dependent band gaps [22]. Some authors have considered isolating in multiple directions simultaneously [23].

Several studies have highlighted that the performance of a QZS isolator is inherently sensitive to small adjustment errors in its static or dynamic stiffnesses [24–26]. As a result many authors have recently began to counter this sensitivity with adjustable devices that can correct such errors [27–31]. Semi-active enhancements to the concept, allowing automatic adjustment to different loads, are also being considered [32], and there has also been an interesting concept that consists of multiple isolators adjusted for varying static loads, to reduce the sensitivity to load error [29,33].

As the limit of zero stiffness is approached, the behaviour becomes increasingly dominated by the dissipative properties of the system, which, in general, are viscous damping and dry friction. Therefore, it becomes important to determine the exact form of the damping, rather than resort to simple linear models. Notably, if the QZS device features mechanical linkages it is likely to

* Corresponding author.
*E-mail address:* a.d.shaw@swansea.ac.uk (A.D. Shaw).

https://doi.org/10.1016/j.ymssp.2024.111113
Received 20 July 2023; Received in revised form 11 December 2023; Accepted 4 January 2024
Available online 7 February 2024

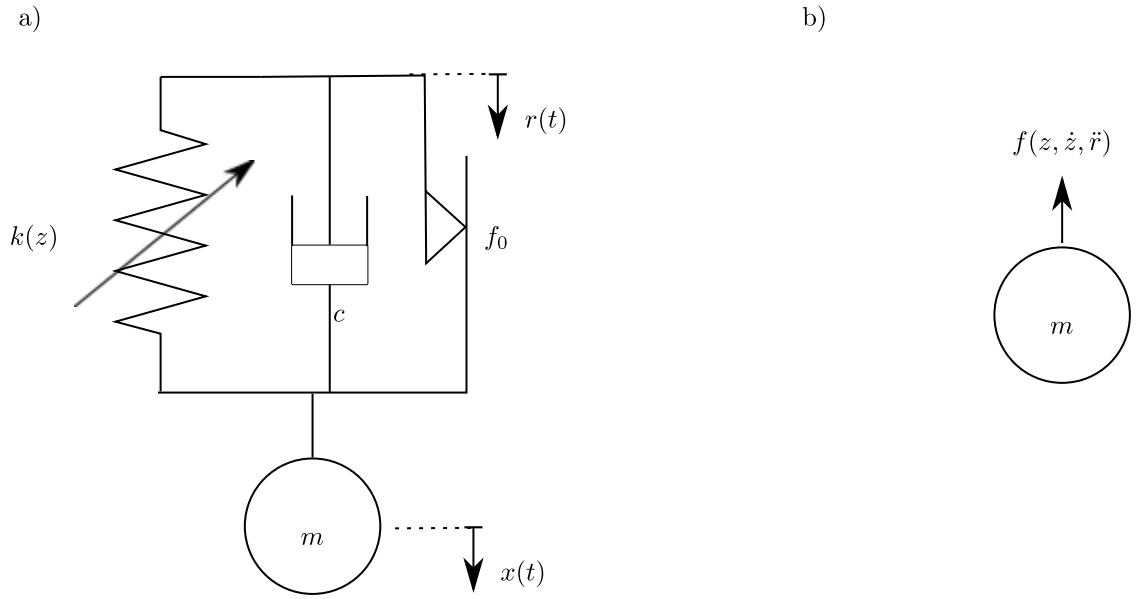


**Fig. 1.** (a) A mass suspended on a nonlinear spring with a frictional damper. (b) Free body diagram of the payload mass.

exhibit some frictional dissipation. Hu and Zhou studied the effect of hysteretic dampers coupled in a nonlinear manner to the payload [34], and also compared the effect of viscous damping, hysteretic damping and hysteretic with geometrically nonlinear coupling both analytically and experimentally [35]. Their analysis predicted rich behaviour including 1/3 subharmonic responses to base excitation, and isolated primary resonances.

A study by Ravindra and Malik [36] used a harmonic balance method to highlight how friction can cause complex responses in a base excited Duffing oscillator with zero linear stiffness, including isolated frequency response curves. This study showed that friction could cause isolated branches of resonance. It also causes the system to lock at low base amplitudes and frequencies, making the property of 'zero stiffness' one that is hard to observe experimentally. Zheng et al. [5] showed that a fractional derivative model most closely matched their 3D printed isolator, and that this significantly altered the shape of the resonant peak.

This paper continues previous work by the authors on a design for a simple QZS device [37,38]. The device acts in tension and allows accurate adjustment of the force displacement curve to correct both loading and stiffness errors, which are known to have increasingly adverse effects on isolation performance as the limit of zero stiffness is approached [24,26]. As such it can make a good claim to being a true experimental implementation of a QZS device. However, directly observing the 'zero frequency' dynamics proves very challenging due to some of the issues above. Instead, the work described in this paper seeks to reproduce the complex dynamics predicted for a QZS device with frictional damping, and then to explore how high frequency motion could potentially be used to release friction and make the low frequency dynamics observable.

The work is structured as follows. Section 2 introduces a single-degree-of-freedom model for the system considered, and this is analysed with the harmonic balance method in Section 3. Section 3 also introduces some more generalized analysis in terms of limit, backbone and breakout curves that gives a broader guide to performance. Section 4 introduces analysis of the effect of high frequency excitation on the low frequency dynamics, deriving an equivalent viscous damping coefficient for a frictional system with high frequency excitation, and demonstrating this. Finally Section 5 gives experimental demonstration of the above and Section 6 draws conclusions.

## 2. Equation of motion

Referring to Fig. 1 the equation of motion is obtained as

$$m\ddot{x} + f(z, \dot{z}, \ddot{r}) = 0\,, \tag{1}$$

or more conveniently

$$m\ddot{z} + f(z, \dot{z}, \ddot{r}) = -m\ddot{r}\,, \tag{2}$$

where $z(t) = x(t) - r(t)$, and $(t)$ has been dropped for brevity.

The restoring force function allows the possibility that the frictional element may lock when velocity is zero and the sum of the other forces is smaller in magnitude than the maximum static friction force [39]. It is given by

$$f(z,\dot{z},\ddot{r}) = \begin{cases} k(z)z + c\dot{z} + f_0\mathrm{sgn}(\dot{z}), \text{ when } \dot{z} \neq 0 \\ k(z)z - f_0\mathrm{sgn}(m\ddot{r} + k(z)z), \text{ when } \dot{z} = 0 \text{ and } |m\ddot{r} + k(z)z| > f_0 \\ -m\ddot{r}, \text{ when } \dot{z} = 0 \text{ and } |m\ddot{r} + k(z)z| \leq f_0 \end{cases} . \tag{3}$$

The first case in Eq. (3) describes the condition when there is sliding within the frictional element. The second describes the instantaneous situation when the relative velocity across the stiffness element is zero, and friction is insufficient to overcome the other forces; at this moment the velocity has no sign so the sum of resultant forces must be used to determine the direction of the friction force. (This is especially important when exiting a period of locking.) The third describes the situation where friction locks the isolator and the mass becomes rigidly connected to the base motion giving $x = r$, $z = 0$.

## 3. Harmonic balance analysis

This analysis mostly follows Ravindra and Mallik [36] to solve the equation describing a base excited Duffing oscillator which has both viscous and Coulomb damping. However, a dimensional form is used and some linear stiffness is included, to accommodate the effect of imperfect adjustment, meaning that this stiffness is not quite zero. Furthermore, the elastic restoring force function is an odd polynomial of 5th order rather than cubic. This is because a 5th order function gives a better match to the shape of the force displacement curve of the experimental device, noting the profound effect that changes in the nonlinear profile can have on the resonance curves of a QZS device [40]. The elastic restoring force term given in Eq. (3) is given by

$$k(z)z = k_1 z + k_3 z^3 + k_5 z^5 \implies k(z) = k_1 + k_3 z^2 + k_5 z^4 . \tag{4}$$

It is assumed that the excitation is due to harmonic base motion described by $r = R\cos(\Omega t - \phi)$, and that the solution is monoharmonic $z = Z\cos(\Omega t)$; where the solution has been time shifted so that the phase $\phi$ appears in the forcing function and not in the response, to simplify analysis. In a Fourier series of one period of $\mathrm{sgn}(\sin\Omega t)$, the fundamental sin component amplitude is $4/\pi$. This can be used to obtain the harmonic balance equations

$$\Omega^2 mR\cos\phi = K(Z)Z - \Omega^2\, mZ \tag{5}$$

$$\Omega^2 mR\sin\phi = -c\Omega Z - 4f_0/\pi , \tag{6}$$

where the amplitude dependent stiffness is given by

$$K(Z) = k_1 + 3k_3 Z^2/4 + 10k_5 Z^4/16 \tag{7}$$

for an odd spring restoring force function up to 5th order [40]. This gives the amplitude equation

$$\Omega^4 m^2\left(Z^2 - R^2\right) + \Omega^2\left(c^2 Z^2 - 2mK(Z)Z^2\right) + 8\Omega Z c f_0/\pi + (K(Z)Z)^2 + (4f_0/\pi)^2 = 0 \tag{8}$$

which can be solved as a polynomial in $\Omega$ for a trial value of $Z$, or vice versa, accepting only positive real solutions. The phase can then be determined using Eqs. (5) and (6).

Once results have been determined in terms of relative displacement $z$, they may be viewed in terms of absolute displacement $x$. This is assumed to be of the form $x = X\cos(\Omega t + \phi_X)$ (to excitation $r = R\cos\Omega t$) where the absolute displacement amplitude may be obtained by

$$X = \sqrt{(R + Z\cos\phi)^2 + (Z\sin\phi)^2}. \tag{9}$$

### 3.1. Backbone curve

At resonance, $\phi = -\pi/2$ so the left side of (5) becomes zero and hence:

$$\Omega = \sqrt{\frac{K(Z)}{m}} \tag{10}$$

which defines the responses of the underlying conservative system, or the so-called backbone curve. Alternatively this can be considered as the amplitude dependent natural frequency of the system.

### 3.2. Limit curve for base excitation

Similarly, when $\phi = -\pi/2$ Eq. (6) becomes:

$$Z = \frac{Rm\Omega}{c} - \frac{4f_0}{\pi\Omega c} \tag{11}$$

which defines the so called limit curve for base excitation. (Note that limit curves have a very different trend under forced excitation [40,41].) This again describes a resonant response, but in terms of nonconservative terms, in contrast with (10) which considers purely conservative terms. This is the maximum amplitude any system could reach for given parameters of friction force,

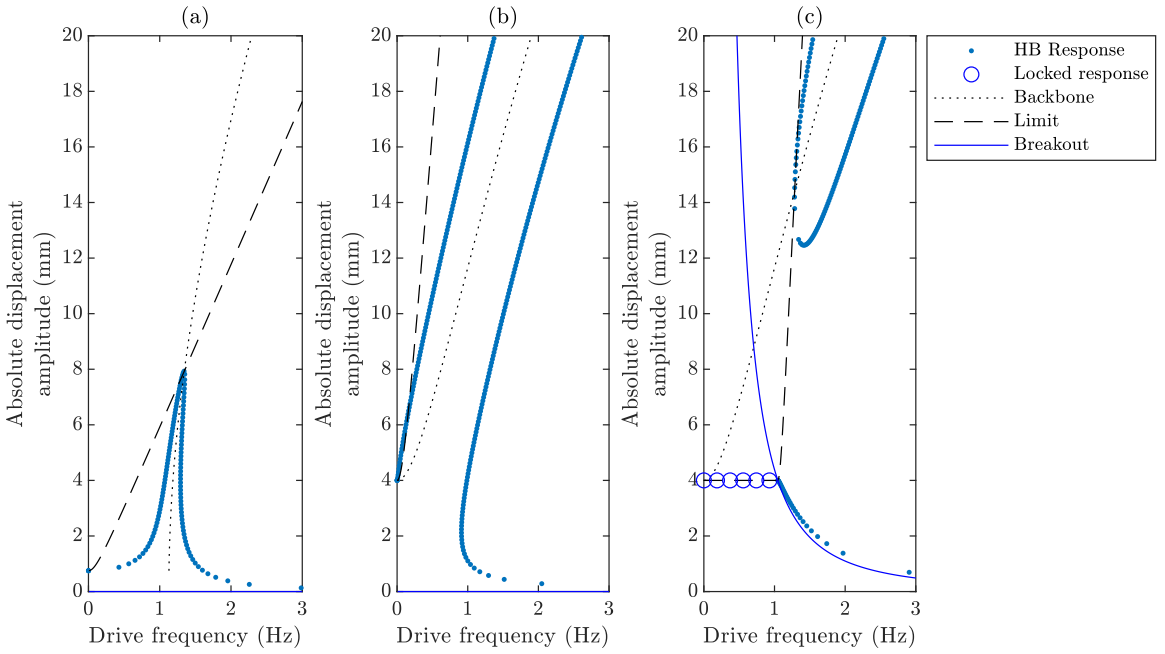


**Fig. 2.** Some typical results of harmonic balance analysis. In all cases $m = 1.47$ kg. (a) $k_1 = 74.0$ N m$^{-1}$, $k_3 = 6.39 \times 10^5$ N m$^{-3}$, $k_5 = 3.91 \times 10^8$ N m$^{-5}$, $c = 1.18$ Nsm$^{-1}$, $f_0 = 0.00$N, $R = 0.75$ mm, (b) $k_1 = 0.00$ N m$^{-1}$, $k_3 = 6.09 \times 10^5$ N m$^{-3}$, $k_5 = 3.73 \times 10^8$ N m$^{-5}$, $c = 1.15$ N s m$^{-1}$, $f_0 = 0.00$ N, $R = 4.00$ mm, (c) is similar to (b) except $f_0 = 0.20$ N.

damping coefficient and excitation amplitude, regardless of $K(Z)$ or mass $m$, because the condition $\phi = -\pi/2$ implies that the elastic and inertial forces cancel each other perfectly. The condition of equations (10) and (11) being satisfied defines a system that is being forced exactly at resonance; the intersection of these two curves on a frequency amplitude plot occurs at the nonlinear resonance peak in a typical stiffening oscillator. Note that in this work, there are also situations where the two curves never meet causing unbounded resonance, and where they meet at the start of an isolated resonance region.

### 3.3. Break-loose curve

It should be noted that if either the excitation frequency or the excitation amplitude are sufficiently small, there is insufficient force to break the static friction within the system, and the isolator will lock; in these cases there is no relative motion between payload and base and $Z = 0$. The threshold for this behaviour can be found by setting $Z$ to zero in equation (11), giving

$$R = \frac{4f_0}{\pi m \Omega^2}. \tag{12}$$

This so-called break-loose curve defines the value of $R$ below which no relative motion will occur at a given $\Omega$, regardless of $c$ or $k(z)$. If rearranged for $\Omega$ it gives the frequency below which no relative motion will occur for a given $R$, known as the break-loose frequency [36]. Alternatively, this relation can be found by seeing that when it is true, equation (8) will have no nonzero terms which do not contain $Z$, hence $Z = 0$ becomes a solution.

### 3.4. Results of harmonic balance analysis

Figure 2 presents some typical scenarios from the above analysis in terms of the resulting absolute response amplitudes, and highlights the potentially complex ways the interactions of backbone, limit and breakout curves can influence the response. The parameters chosen are approximate typical parameters found in the experiment described in Section 5, but adapted to highlight various possible behaviours of the system. Fig. 2(a) shows a classic nonlinear stiffening response, where the peak response occurs at the intersection of the backbone and limit curves. The breakout curve is trivial in this case because there is zero friction. In Fig. 2(b) again there is no friction, but there is a QZS response where the backbone starts at zero frequency. In addition there is greater forcing, and due to a combination of this and the stiffening nonlinearity, the backbone curve never meets the limit curve so the response is unbounded. With the introduction of friction, Fig. 2(c) shows that the response is locked to the base until the limit curve falls below 4 mm, and then the limit curve begins to rise with frequency. In this situation, the backbone curve remains above the limit curve until approximately 1.2 Hz, where an isolated response branch begins.

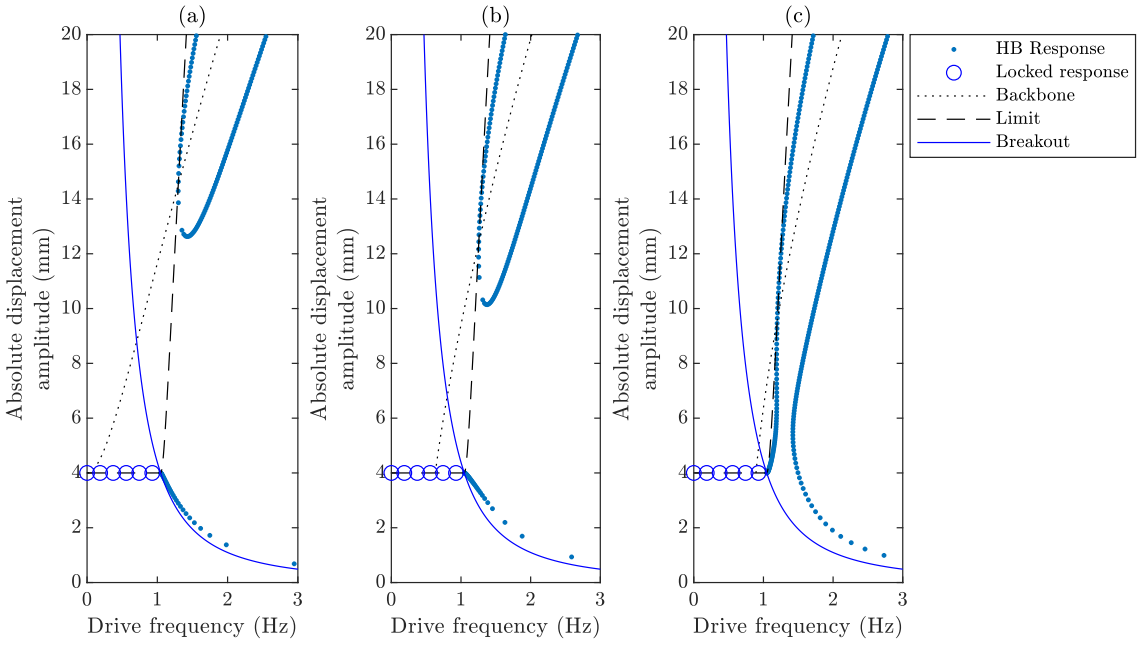


**Fig. 3.** The effect of increasing the linear stiffness. In all cases $m = 1.47$ kg, $c = 1.2$ Nsm$^{-1}$, $f_0 = 0.20$ N, $R = 4.00$ mm. (a) $k_1 = 0.00$ N m$^{-1}$, $k_3 = 6.09\times10^5$ N m$^{-3}$, $k_5 = 3.73\times10^8$ N m$^{-5}$, (b) $k_1 = 23.1$ N m$^{-1}$, $k_3 = 6.18\times10^5$ N m$^{-3}$, $k_5 = 3.79\times10^8$ N m$^{-5}$, (c) $k_1 = 46.3$ N m$^{-1}$, $k_3 = 6.28\times10^5$ N m$^{-3}$, $k_5 = 3.84\times10^8$ N m$^{-5}$.

Figure 3 shows that the system response can be highly sensitive to the errors that cause the low level stiffness of the QZS to be slightly above zero. Note that in practice it is very hard to achieve a perfectly zero stiffness. The linear component of stiffness increases successively from Fig. 3(a) to Fig. 3(c), causing the base of the backbone to move to the right. This causes it to cross the limit curve at a lower amplitude, firstly bringing the isolated branch nearer to the non-resonant branch as seen in Fig. 3(b), and then joining the resonant and non-resonant branches as seen in Fig. 3 (c). Note that the linear stiffness in Fig. 3 (c) is still very low in the context of the mass that is supported. However, this small increase in stiffness is sufficient to change the response from an isolated resonance, to one where stepping up in frequency is guaranteed to cause the response to jump up to the resonant branch, and become unbounded if frequency continues to rise.

Finally, Fig. 4 shows the effect of increasing the excitation amplitude on the system response. Firstly, this brings the isolated region nearer to the non-resonant region, then the regions become connected. Then, as the excitation amplitude increases, the upper and lower jump frequencies become further apart.

These results have highlighted the complex interactions that can lead to very different qualitative responses in a QZS device with friction. These pose substantial practical problems because small changes in damping and friction can have profound effects, and these properties can be hard to measure or control. Furthermore, the response is very sensitive to the low amplitude shape of the backbone, and as shall be seen it can be hard to measure this directly or the quasi-static stiffness profile that will determine it. An experimental demonstration of the system behaviour, with comparison to this analysis, is given in Section 5.2.

### *3.5. Displacement transmissibility and isolation performance of the frictional QZS device*

Transmissibility is a widely used measure to evaluate QZS devices, particularly when they are being used for the purpose of vibration isolation, so this section gives some results in terms of transmissibility and also discusses the general effect of friction when vibration isolation is the aim. Fig. 5 displays the absolute response, displacement transmissibility magnitude $T_r = X/R$ and relative phase $\phi$ for two QZS systems which are identical except that one is frictionless while the other is not, considering two different base amplitudes. Note that this isolator has imperfect stiffness adjustment, giving $k_1 = 37.0$ N m$^{-1}$, which would give a linear natural frequency of 0.80 Hz if nonlinearity and damping were neglected.

Firstly, considering the response without friction shown in Fig. 5(a,c,e), it may be seen that the transmissibility is a somewhat unreliable guide to performance in the resonant region because it varies substantially with the excitation level. Indeed, the absolute response amplitude is a more consistent guide to performance, because the response amplitudes are so heavily influenced by the path of the backbone curve which only varies slightly in absolute terms between the two systems. However, in the isolation region, nonlinearity is limited, and the two systems' transmissibilities are quite similar, with the greater excitation amplitude giving slightly greater transmissibility. At higher frequencies the transmissibility in the isolation region converges to linear-like behaviour where transmissibility is independent of excitation amplitude.

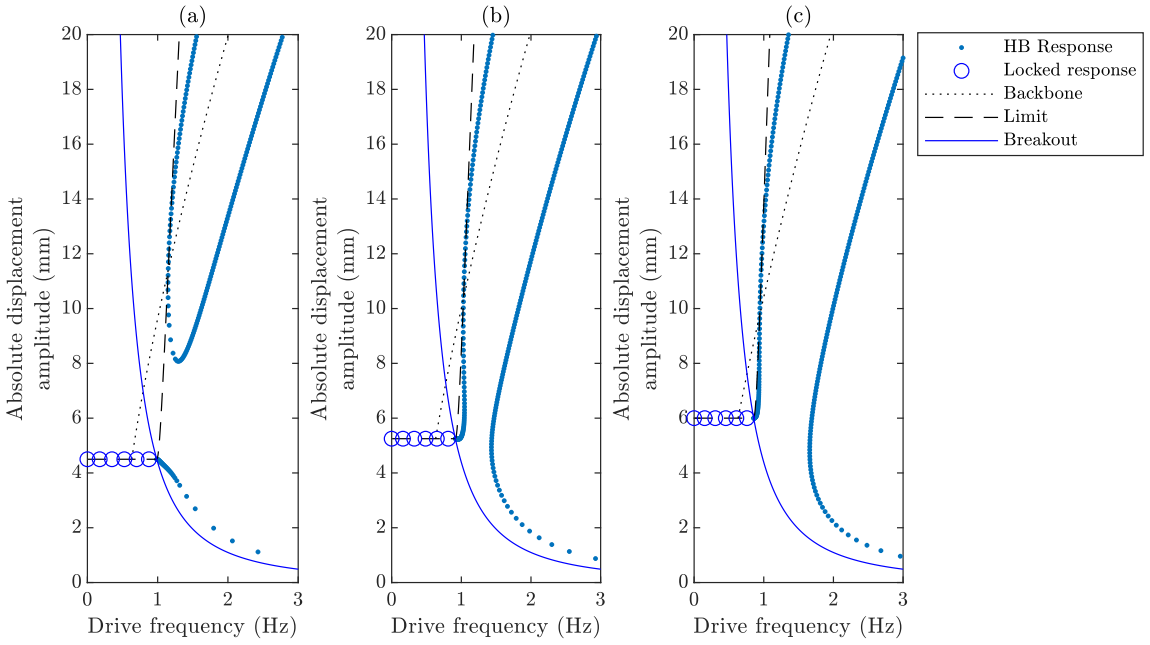


**Fig. 4.** The effect of increasing the base amplitude. In all cases $m = 1.47$ kg, $c = 1.2$ N s m$^{-1}$, $f_0 = 0.20$ N, $k_1 = 23.1$ N m$^{-1}$, $k_3 = 6.18\times10^5$ N m$^{-3}$, $k_5 = 3.79\times10^8$ N m$^{-5}$ (a) $R = 4.50$ mm, (b) $R = 5.25$ mm, (c) $R = 6.00$ mm.

When the device with friction (Fig. 5 (b,d,f)) is considered, it is seen to have a response amplitude similar to the frictionless system at high response amplitudes, when the friction becomes less significant. However, lower amplitudes in the resonant region are radically different to the frictionless system due to the existence of the break-loose frequency, and in the case $R = 3.0$ mm this causes the resonant branch to become isolated from the low amplitude response. Clearly transmissibility is an even less consistent measure in the presence of friction, because it varies so drastically with excitation amplitude. However, when considering the isolation region there an opposite trend to the frictionless system where the transmissibility is greater for a smaller excitation amplitude. This is because friction introduces a nonlinearity that remains significant at low response amplitudes, in contrast to stiffness nonlinearity. More specifically, it may be seen that the final term of Eq. (8) is independent of both base and response amplitude. Therefore as the base excitation amplitude falls, this term becomes more significant causing the transmissibility to rise. So when friction is present, tramsissibility becomes significantly base-amplitude dependent in the isolation region as well as in the resonant region.

The isolation performance may be compared in the resonant region and the isolation region separately. In the resonant region, and at frequencies below this, friction is advantageous, because friction locking prevents the small gains seen at low frequencies in the frictionless system. More significantly, it can act to detach the unbounded resonant region at low excitation amplitudes, which could be highly beneficial in any situation where the excitation frequency rises from zero, such as when a motor spins up to speed. However, friction is clearly undesirable in the isolation region, where Fig. 5 shows that the frictional QZS has significantly greater response in terms of both absolute amplitude and displacement transmissibility. This would appear to be related both to the direct effect of friction giving an additional means of transmitting vibration forces to the payload, and to the presence of the break-loose frequency which acts to increase the frequency at which the roll-off in amplitude begins. The phase plots in Fig. 5 (e,f) give further insight, as it can be seen that the phase in the isolation region for the frictional isolator converges to the high frequency asymptote of $= -\pi/$ far more slowly than the frictionless isolator, and this effect is even more pronounced at low excitation amplitude.

### 3.6. Validation of the HB analysis

The presented system features both smooth stiffness nonlinearity and non-smooth frictional nonlinearity, and therefore responses are potentially more complex than the simple monoharmonic responses assumed by the harmonic balance method. This is explored in Fig. 6 which presents results in terms of velocity in order to make any higher harmonics in the response more apparent than if displacement was considered. For all the cases marked with dots in the left hand plot, a time simulation has been launched with initial conditions based on the harmonic balance solution. This time simulation exploits event detection to accurately locate transitions between positive sliding, negative sliding, and locked behaviour, and therefore applies the dry friction force accurately with no need for smoothing functions. Circles on the left hand plot indicate the fundamental amplitude extracted from a Fast Fourier Transform (FFT) of one period of the time simulation, taken after 20 periods of settling time. The FFT used 32768 points, which was verified to be sufficient to closely match the simulation in all cases.

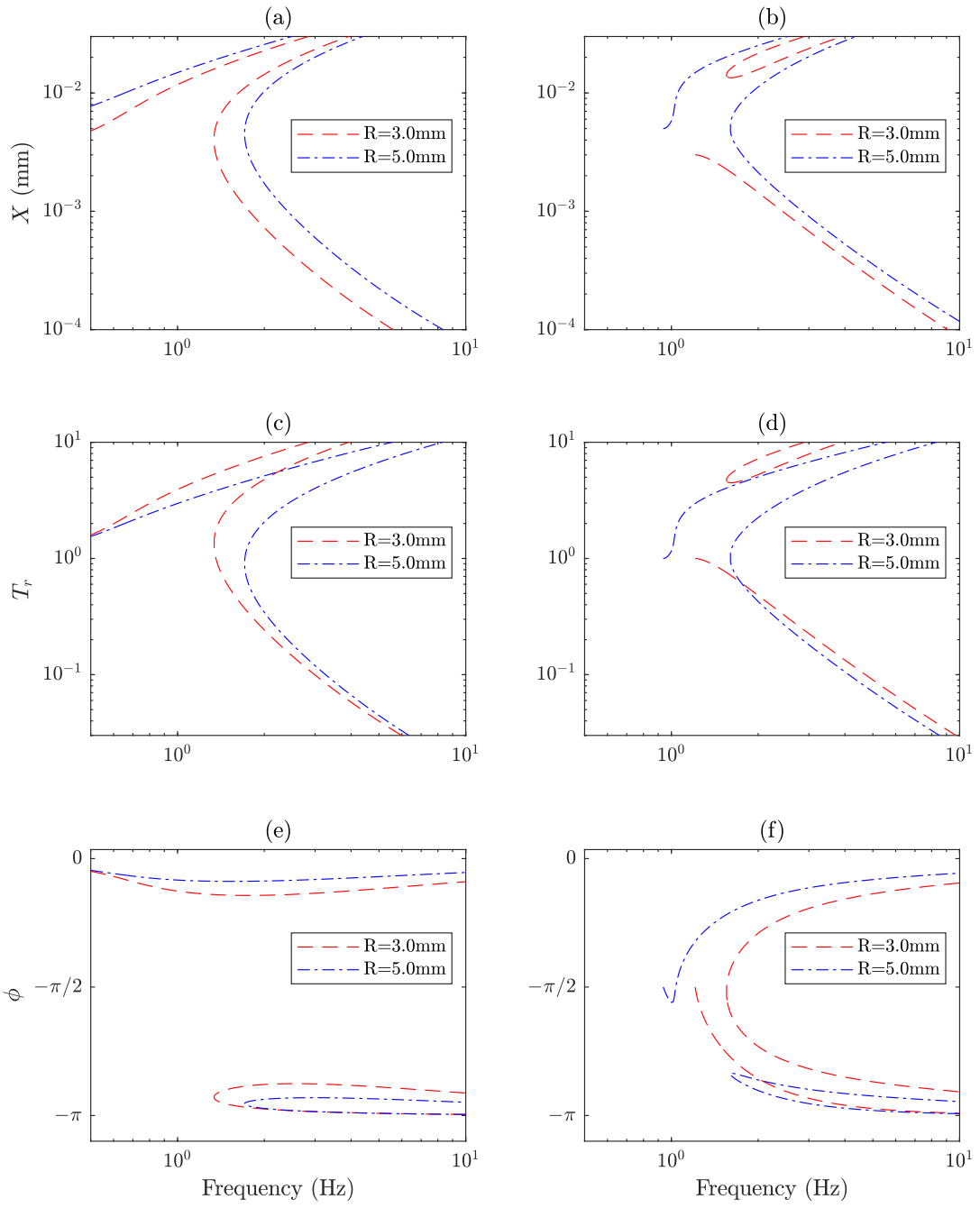


**Fig. 5.** Absolute displacement response amplitude $X$ (a,b), absolute displacement transmissibility amplitude (c,d), and relative displacement phase plots (e,f) for QZS systems at two amplitudes of base excitation. The system parameters are $m = 1.47$ kg, $c = 1.2$ N s m$^{-1}$, $k_1 = 37.0$ N m$^{-1}$, $k_3 = 2.41\times10^{4}$ N m$^{-3}$, $k_5 = 3.82\times10^{8}$ N m$^{-5}$. For the left hand plots (a,c,e), $f_0 = 0.0$ N. For the right hand plots (b,d,f), $f_0 = 0.2$ N. Locked responses are excluded from these results for clarity, noting that when locked $X = R$ hence $T_r = 1$, $Z = 0$ and $\phi$ is undefined.

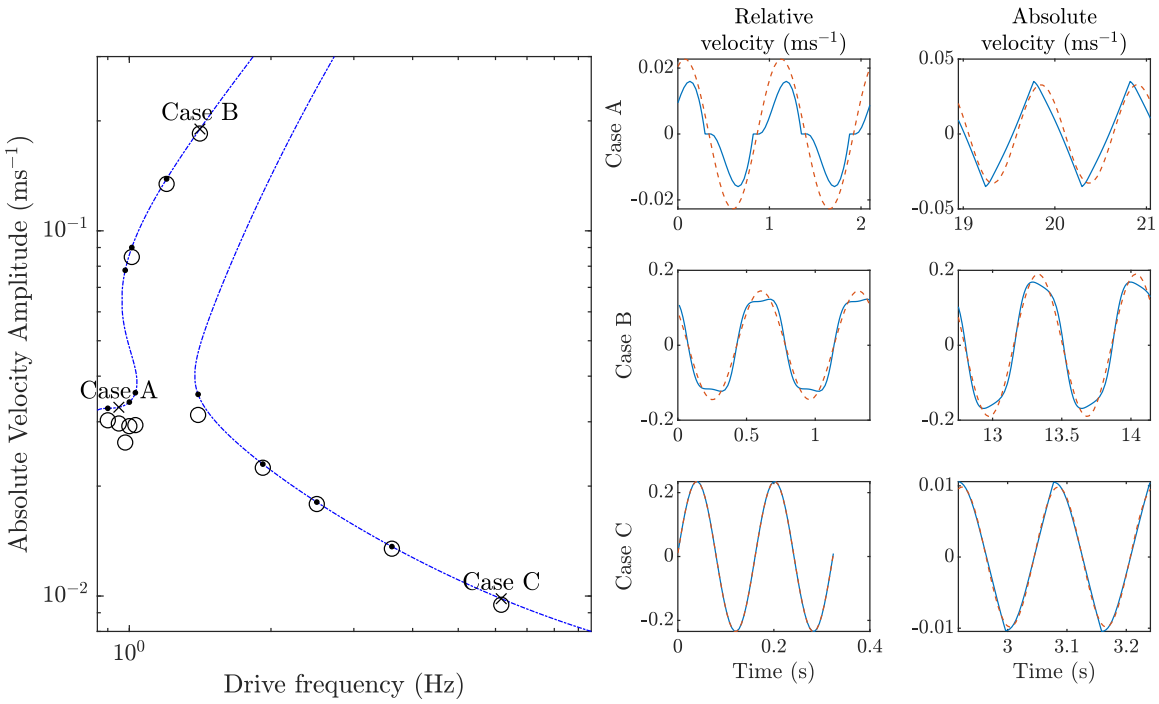


**Fig. 6.** Velocity responses of an QZS device with friction, with properties $m = 1.47$ kg $k_1 = 9.26$ N m$^{-1}$, $k_3 = 6.13 \times 10^5$ N m$^{-3}$, $k_5 = 3.75 \times 10^8$ N m$^{-5}$, $c = 1.2$ N s m$^{-1}$, $f_0 = 0.20$ N, and $R = 6.0$ mm. In the left hand plot, the blue line indicates harmonic balance solutions, with black dots indicating particular solutions that have been validated with time simulations. Crosses indicate the 3 cases where simulated time series data is presented in the panels on the right. Circles indicate the fundamental amplitude extracted by FFT from the time simulation. In the time series plots, the solid line shows the result of time simulation, while the dashed line shows the monoharmonic response calculated by harmonic balance for comparison.

The results show that the assumption of monoharmonic response is not strictly true, but depending on the operating regime and the result of interest, the accuracy is generally quite reasonable. In the vicinity of Case A, the accuracy is poorest. This is very near the break-loose frequency, and the relative velocity plot shows quite a complex response with brief periods of friction locking. It is therefore unsurprising that the amplitudes predicted by harmonic balance show some inaccuracy in this region.

In the high amplitude resonant region as typified by Case B, the effect of the stiffness nonlinearity in adding harmonic distortion is clearly visible in the time series, however the HB predictions are generally quite accurate.

The accuracy is very good in the isolation region, where case C shows that the harmonic balance solution does a near perfect job of predicting the relative velocity response. However, some small deviations from the harmonic balance prediction are visible in absolute velocity response. This is probably due to the fact that while the relative velocity amplitude tends toward the base excitation velocity amplitude at high frequency, the absolute velocity amplitude tends to zero. Hence small distortions due to nonlinearity that are insignificant to the relative response may be more significant in the absolute response.

Figure 6 also shows that the amplitude predictions of the harmonic balance method become less accurate in the vicinity of bifurcations; however it seems to provide good indications of the frequencies where jumps or drops occur.

## 4. Effect of high frequency excitation on low frequency response

A problem highlighted in Section 3.4 is that it very hard to observe the dynamics of a near-zero natural frequency in a stepped sine type experiment, because the forced response at low frequency is either locked by friction, or requires a very high base excitation. A potential solution is to 'break' the friction locking, through the use of some high frequency forcing that prevents locking but does not particularly affect the low frequency dynamics. The free responses of the QZS system can then be observed to gain insights about its performance. The high frequency excitation could be supplied in numerous ways, for example through piezoelectric actuators, but in this case it is supplied through base excitation for convenience.

To analyse this situation, it is assumed that base excitation frequency $\Omega$ is much higher than the nonlinear natural frequency of the system. Furthermore, Eq. (2) can be approximated over a short time period of the order of $2\pi/\Omega$ and in the vicinity of a displacement $z^*$ as

$$m\ddot{z} + c\dot{z} + k(z^*)z + f_0\mathrm{sgn}(\dot{z}) = \Omega^2 mR\cos\Omega t. \tag{13}$$

Equation (13) can be thought of as Eq. (2) with the restoring force as described in case 1 of equation Eq. (3) with the approximation $k(z) \approx k(z^*)$. This approximation is reasonable over the brief time period of $2\pi/\Omega$ because the displacement $z$ only changes slowly

due to the near zero nonlinear natural frequencies of the QZS system. It is also assumed that the excitation is sufficient to unlock the system, hence the possibility of sticking is neglected.

Over a period where there are no changes in sign of the relative velocity, Eq. (13) is solved to give

$$z = \mathrm{e}^{-\zeta\omega_{nz^*}t}\left(A\cos\omega_{dz^*}t + B\sin\omega_{dz^*}t\right) - f_0\mathrm{sgn}(\dot{z})/k(z^*) + Z\cos(\Omega t+\phi)\,, \tag{14}$$

where $\zeta = \frac{c}{2\sqrt{mk(z^*)}}$, $\omega_{nz^*} = \sqrt{\frac{k(z^*)}{m}}$, $\omega_{dz^*} = \omega_{nz^*}\sqrt{1-\zeta^2}$, $A$ and $B$ are determined by initial conditions,

$$Z = \frac{R}{\sqrt{\left(1-\frac{\omega_{nz^*}^2}{\Omega^2}\right)^2 + \left(2\zeta\omega_{nz^*}/\Omega\right)^2}} = \frac{\Omega^2\, mR}{\sqrt{\left(\Omega^2 m - k(z^*)\right)^2 + (\Omega c)^2}}\,, \tag{15}$$

and

$$\tan\phi = \frac{2\zeta\Omega\omega_{nz^*}}{\Omega^2-\omega_{nz^*}^2}. \tag{16}$$

Equation (14) is an approximate solution to the transient dynamics of equation (2) subject to high frequency excitation, valid over a short time only, but is sufficient to illustrate that over periods where $\mathrm{sgn}(\dot{z})$ is constant, the high frequency dynamics due to excitation, and the low frequency dynamics of the underlying system, are effectively decoupled; the high frequency effects are solely contained in the final term. The situation of mostly constant $\mathrm{sgn}(\dot{z})$ occurs when the relative velocities due to the low frequency dynamics are high, compared to those caused by high frequency excitation. The relative velocity amplitude due to the high frequency excitation is given by

$$V = \Omega Z\,. \tag{17}$$

In summary, when the velocity amplitude of free response is large compared to $V$, the high frequency excitation has little effect on the low frequency response.

A very different situation occurs when the high frequency excitation results in a velocity that is greater than that due to low frequency motion. In this situation, the high frequency response causes rapid switching of the sign of $f_0\mathrm{sgn}(\dot{z})$. To understand the effect of this on the low frequency dynamics, the effect of the rapidly changing friction force can be time averaged over a period $\frac{2\pi}{\Omega}$. A further assumption is made that the relative velocity can be approximated as

$$\dot{z} \approx \bar{v} + V\cos\Omega t. \tag{18}$$

where $\bar{v}$ is the velocity due to low frequency motion, that is assumed to remain constant over a single period of high frequency excitation, and the phase lag has been neglected for convenience without loss of generality.

Recall that for relative velocity to change sign in the period, $\bar{v} < V$. The time averaged force generated by the friction term over a cycle of excitation $\bar{f_c}$, is evaluated as follows:

$$\bar{f_c} = \frac{\Omega}{2\pi}\int_0^{\frac{2\pi}{\Omega}} f_0\mathrm{sgn}(\dot{z})\,\mathrm{d}t = \frac{f_0}{\pi}\left(\int_0^{\phi^*}\mathrm{d}\phi - \int_{\phi^*}^{\pi}\mathrm{d}\phi\right) = \frac{f_0}{\pi}\left(2\phi^*-\pi\right) \tag{19}$$

where $\phi = \Omega t$ and $\phi^*$ denotes the point in the cycle where relative velocity crosses zero given by $\phi^* = \cos^{-1}\left(\frac{-\bar{v}}{V}\right)$. A graphical indication of the various terms used in this calculation is given in Fig. 7.

Noting that $\frac{\bar{v}}{V} < 1$ due to the assumptions, the value $\phi^*$ can be expanded to give

$$\begin{aligned}\phi^* = \cos^{-1}\left(\frac{-\bar{v}}{V}\right) &= \pi/2 + \sum_{n=0}^{\infty}\frac{(2n)!}{2^{2n}(n!)^2}\frac{(\bar{v}/V)^{2n+1}}{2n+1}\\ &= \pi/2 + (\bar{v}/V) + \frac{(\bar{v}/V)^3}{6} + \frac{3\,(\bar{v}/V)^5}{40} + \frac{15\,(\bar{v}/V)^7}{336}\ \ldots\end{aligned} \tag{20}$$

Noting that the higher order terms in Eq. (20) rapidly become negligible as $\bar{v} \ll V$, only the first two terms are substituted into Eq. (19) to give:

$$\bar{f_c} \approx \frac{2f_0}{\pi}\left(\bar{v}/V\right) + \mathcal{O}\left((\bar{v}/V)^3\right). \tag{21}$$

This can be thought of as an equivalent linear damping coefficient $\bar{c}$ applied to the low frequency dynamics represented by $\bar{v}$. Substitution of Eqs. (15) and (17) results in $\bar{f_c} = \bar{c}\bar{v}$ where

$$\bar{c} = \frac{2f_0}{V\pi} = \frac{2f_0\sqrt{1+\left(\frac{c}{\Omega m}\right)^2}}{\pi R\Omega}\,, \tag{22}$$

where $k(z^*)$ has been neglected, because it can be seen from Eq. (15) that it is insignificant due to the assumption that $\Omega$ is well above the resonant frequency of the system.

Figure 8 shows time series of an initially displaced QZS system with base excitation. This is created with a time simulation that uses event detection to accurately locate the changes in the sign of relative velocity, and alter the direction of friction force

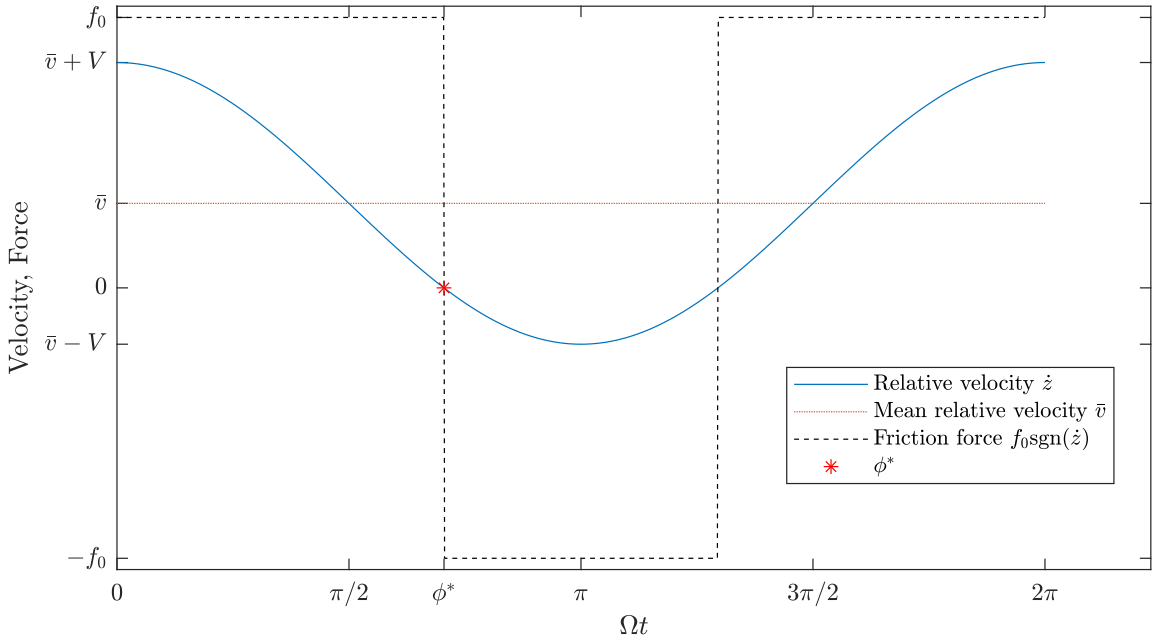


**Fig. 7.** Illustration of terms in Eq. (19).

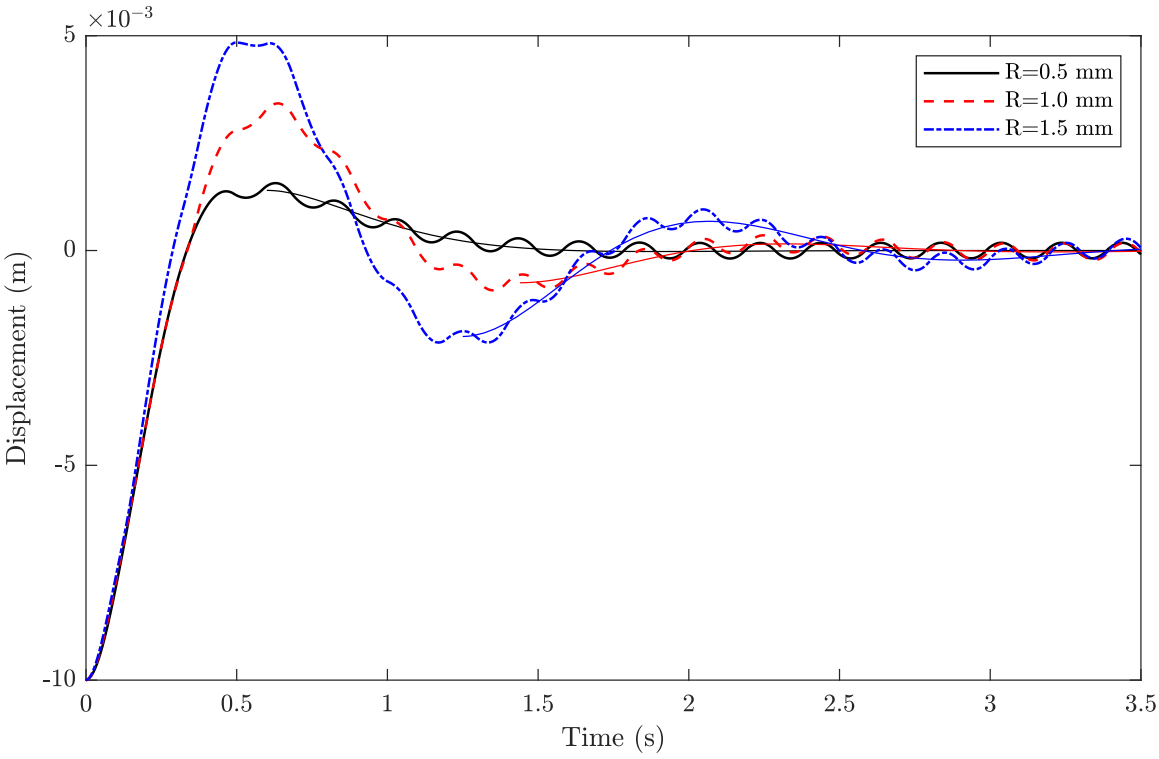


**Fig. 8.** Simulated free decay behaviour of a QZS system with base excitation at 5 Hz and the amplitudes shown. Thin solid lines show response of the equivalent viscously damped system given by Eq. (23). $m = 1.47$ kg, $c = 1.2$ N s m$^{-1}$, $f_0 = 0.20$ N, $k_1 = 23.1$ N m$^{-1}$, $k_3 = 6.18 \times 10^5$ N m$^{-3}$, $k_5 = 3.79 \times 10^8$ N m$^{-5}$.

accordingly. As expected, there is a brief period where the systems behave quite similarly due to all having high velocity, and therefore the excitation and free motions have little interaction. However, as the velocity reduces to zero, the damping effect becomes evident. For the lowest level base excitation, the equivalent damping coefficient is high enough to over-damp the low

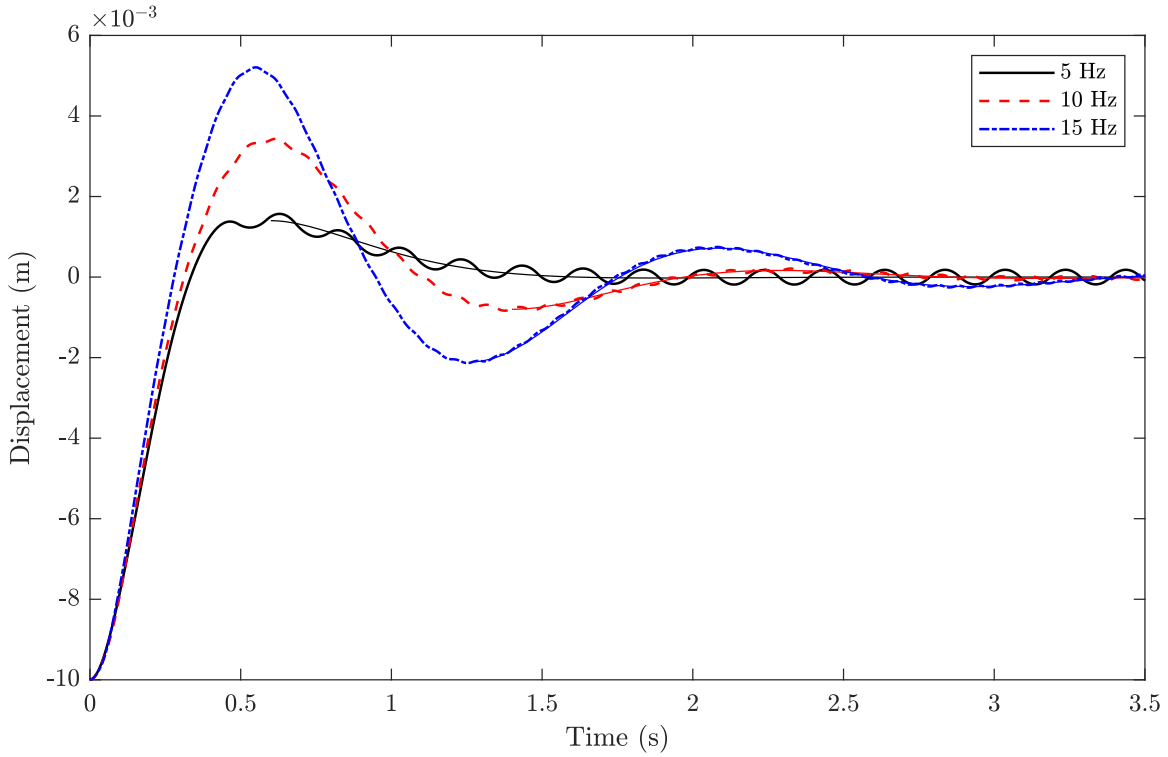


**Fig. 9.** Simulated free decay behaviour of a QZS system with base excitation with $R = 1$ mm and varying frequency. The thin solid lines show the results for the equivalent unexcited viscously damped system. $m = 1.47$ kg, $c = 1.2$ N s m$^{-1}$, $f_0 = 0.20$ N, $k_1 = 23.1$ N m$^{-1}$, $k_3 = 6.18 \times 10^5$ N m$^{-3}$, $k_5 = 3.79 \times 10^8$ N m$^{-5}$.

frequency dynamics, as no further low frequency oscillations are seen. As the base amplitude is increased, the damping reduces and the mass takes longer to settle to a steady state response. The thin solid lines in Fig. 8 show the results of simulating the equivalent unexcited viscously damped system given by

$$m\ddot{z} + (c + \bar{c})\dot{z} + k(z)z = 0 \tag{23}$$

where $\bar{c}$ is calculated using Eq. (22) and other symbols are as defined in Eq. (2). The simulations are chosen to start shortly after the sign of the relative velocity starts to alternate regularly, with the initial condition chosen to roughly match the central trend full frictional simulation. As can be seen, the equivalent viscous system matches the central trend of the friction simulation very well.

The effect of changing the excitation frequency is seen in Fig. 9, where increasing frequency causes a progressively lower damping coefficient as predicted by Eq. (22). Again, a thin solid line indicates the equivalent viscous system response, and the results match closely.

## 5. Experiments

### 5.1. Method

Figure 10 shows the experimental equipment. A mass is suspended via dyneema cord from the nonlinear QZS device. This in turn is suspended from an APS420 ELECTRO-SEIS® long-stroke vibration exciter, configured to vibrate vertically. The vertical shaker motion and that of the payload are measured using both piezoelectric accelerometers and Omron ZX2-LD100 laser displacement sensors. The system is driven by a bespoke signal generator and data acquisition system implemented on a National Instruments CRio-9024 system. The signal generator creates periodic voltage signals based on Fourier series terms up to the third harmonic of the fundamental frequency. This in turn is controlled by routines implemented in Matlab that collect the returning data signals, and automatically seek voltage outputs that lead to purely sinusoidal base motions of the desired amplitude. As seen in Eq. (2), the base excitation is due to the acceleration signal of the base so the accelerometer signals were used to correct the harmonics. However, the laser displacement sensors were used to control the fundamental amplitude, as the fundamental frequency was often too low to get reliable performance from the accelerometers.

The QZS device is described in [37,38]. Briefly, it features two adjustable springs to allow for accurate correction of both loading errors and stiffness errors that can cause significant detriment to the performance of QZS isolators [26]. The vertical spring supports the static weight, and adjusting the preload in this spring precisely adjusts the device so that the equilibrium position occurs at the

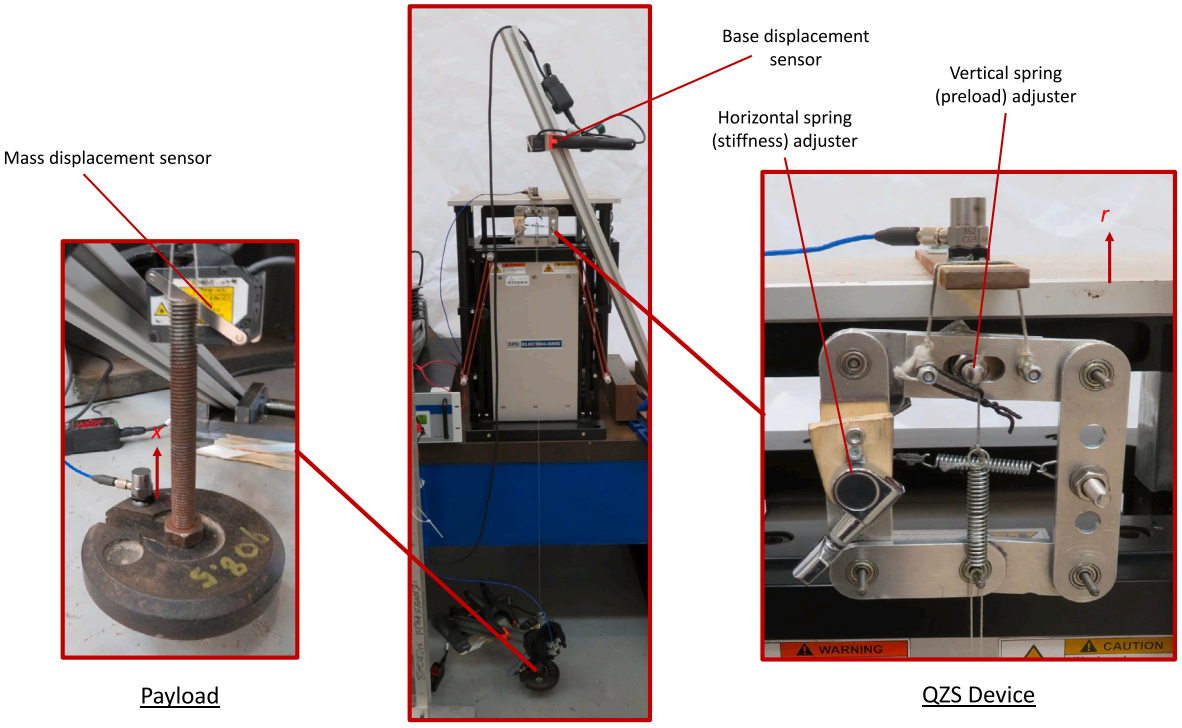


**Fig. 10.** The experimental rig showing payload (left), full apparatus including APS420 shaker (centre), and QZS device (right).

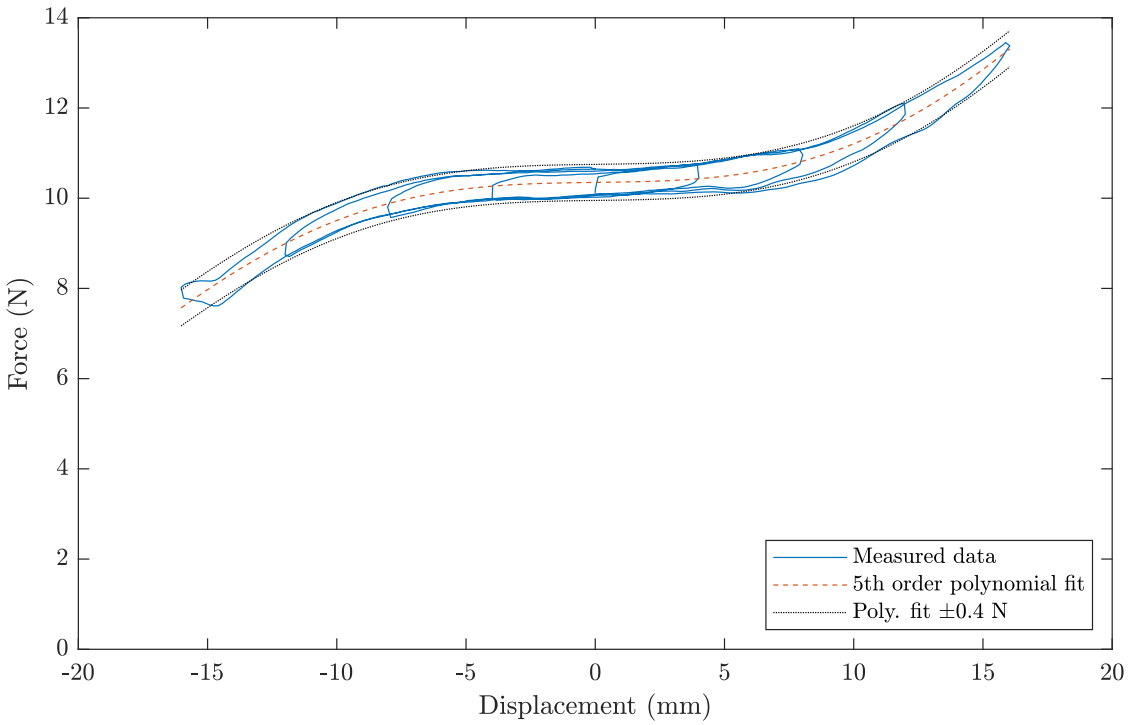


**Fig. 11.** A typical force displacement measurement.

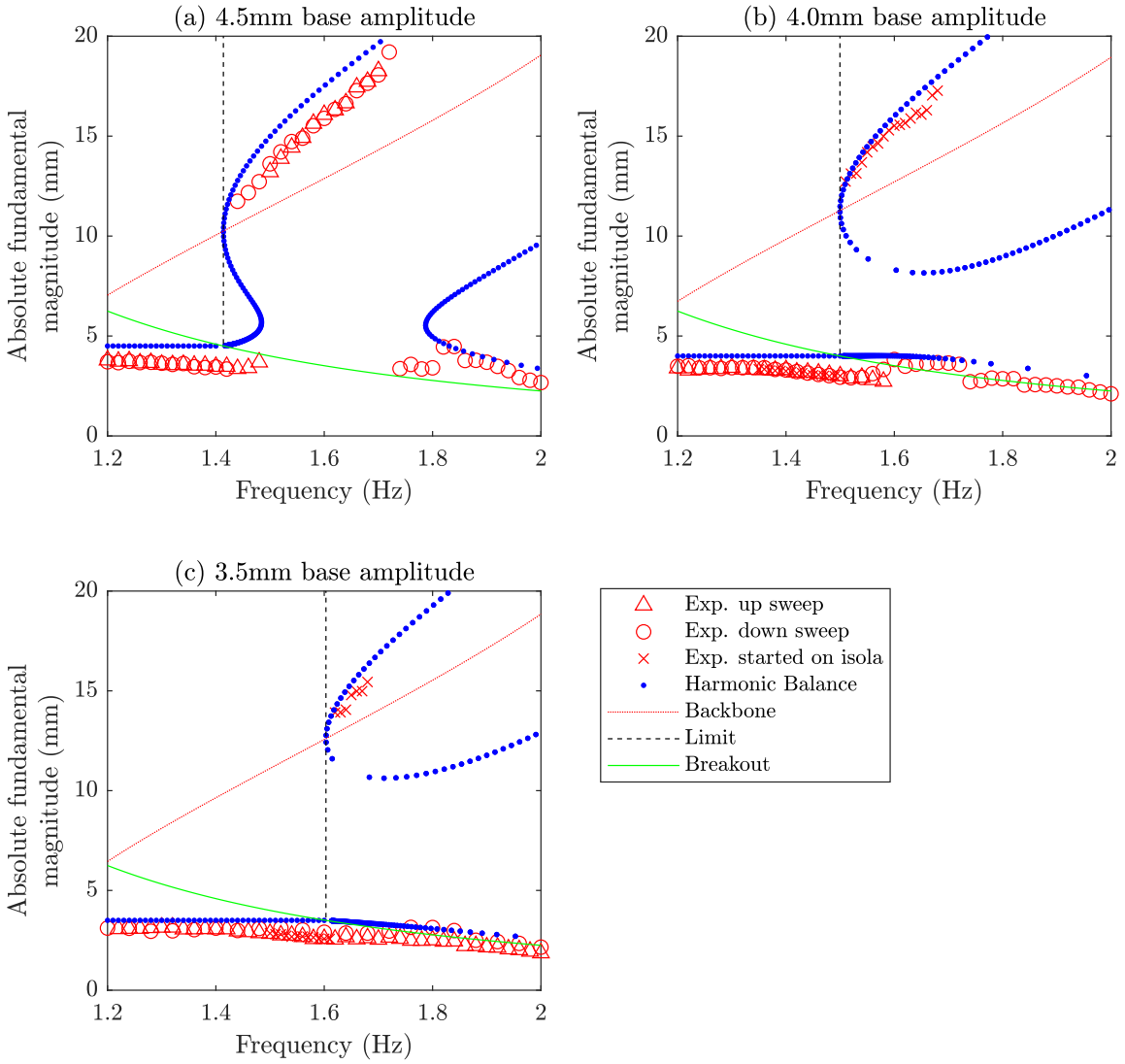


**Fig. 12.** Experimental stepped sine test results, superimposed on analytical results.

point of minimum stiffness. Tension in the horizontal spring causes the lower linkages to buckle and form a snap-through mechanism, inducing negative stiffness. Careful adjustment of this tension allows the negative stiffness to exactly match the positive stiffness of the vertical spring, so that the combined effect is zero stiffness. Both springs are adjusted through the use of tuning pegs typically used on guitars to give precise and backlash free control of the tension. The adjustment of the vertical spring could be performed while the device was on the shaker, by ensuring that the two lower bars of the isolator were horizontal in the static equilibrium position. However, in order to adjust for zero stiffness, the isolator was transferred to a static load testing machine, the measured force displacement curve was inspected and the horizontal spring adjusted as needed. This was repeated periodically during the testing campaign.

Figure 11 shows a typical force displacement curve for the isolator. The load test program began at zero displacement with the isolator positioned at its ideal equilibrium position (with both lower arms horizontal). The tester then performed a series of successively larger up-down sweeps. Fig. 11 shows that the isolator achieves a very low stiffness. It can be seen that the loading and unloading cycles create hysteresis loops; this is due to the presence of friction within the system. The increasing displacement path is approximately 0.8 N above the decreasing displacement path, which is assumed to be due to a 0.4 N friction force acting in the direction opposing the motion. Fig. 11 also shows that a 5th order polynomial fit captures the central trend of the data well, and that when this line is translated upwards or downwards by 0.4 N, there is a reasonable fit to the measured data confirming the assumed friction model. The slight wiggle at −15mm displacement is caused by the displacement being sufficient to cause the vertical spring to slacken slightly, hence indicating the useable relative displacement range of the device.

**Table 1**
Data used for analytical results in Fig. 12.

| Parameter | Value |
|---|---|
| $m$ | 1.47 kg |
| $k_1$ | 65.3 N m$^{-1}$ |
| $k_3$ | $8.47 \times 10^5$ N m$^{-3}$ |
| $k_5$ | $-6.92 \times 10^8$ N m$^{-5}$ |
| $c$ | 0 N s m$^{-1}$ |
| $f_0$ | 0.41 N |

### 5.2. Base amplitude controlled frequency sweeps

These tests consisted of base excitation stepped sine tests; for each data point, the frequency was set, and the control system automatically sought the correct base amplitude and corrected any harmonics in the base motion, before the steady state response was sampled. Initial conditions have an important effect on the steady state response of a nonlinear systems such as this one, so different sequences for collecting data are presented in Fig. 12.

Figure 12(a) shows a case where the base excitation causes a region of unconditionally resonant response (the response always jumps up) between 1.46 Hz and 1.74 Hz. Both the up sweep and the down sweep result in resonant responses. The up sweep was terminated at 1.7 Hz, because if it continued it would increase in amplitude until the device range was exceeded.

Figure 12(b) shows that with a minor reduction in base amplitude, the response to a simple down sweep (from zero initial conditions) now sees no obvious resonance. The up sweep again shows no sign of resonance and is set to continue along a similar curve to the down sweep into the higher frequency region. However, the up sweep was terminated in the interest of time, because the control algorithm was struggling to achieve the required monoharmonic base motion in this region. The × markers in Fig. 12(b) show a sweep where the initial conditions have been forced to trigger the isolated resonant response. The system was initially excited at a base amplitude of 5 mm at 1.7 Hz, triggering the resonant response. The base amplitude was then reduced to 4 mm and the sweep proceeded downwards in frequency. The response is seen to proceed along an isolated resonance until it drops down at approximately 1.5 Hz.

Figure 12(c) shows a similar result to (b), however the base amplitude was now 3.5 mm and the lower end of the isola is now at the higher frequency approximately 1.6 Hz. Furthermore, it is clear to see that both the up and down sweeps pass cleanly underneath the isola.

In all experimental cases, a region of friction locked response was observed, to the left of the limit curves shown in Fig. 12 (a-c). However, the measured base amplitudes do not exactly match the base amplitude as expected; this is attributed to the experimental assembly not being perfectly rigid due to features such as joints and the cord used to suspend the payload.

The results in Fig. 12 are superimposed with analytical results from Section 3. The parameters for the analysis are given in Table 1. The payload mass $M$ was measured with digital scales. The nonlinear stiffness parameters $k_3$ and $k_5$ were found by fitting a polynomial to the measured force displacement data using linear regression. The remaining parameters were fitted manually; it was found that the viscous damping $c$ had little effect on the response, perhaps due to the very low frequencies involved, so it was set to zero. The frictional force $f_0$ was seen to be in the range expected from the measured quasi-static force displacement data, as shown in Fig. 11. Note that with zero viscous damping, the limit curves in Fig. 12 are vertical, and the dropdown and breakout frequencies are determined by the friction force. The linear stiffness $k_1$ was initially taken from a polynomial fit of the measured quasi-static data to be 7.25 N m$^{-1}$. However, to obtain a good fit to the experimental data the much higher value given in Table 1 was required. This suggests that some loss of adjustment was experienced moving the isolator between the quasi-static and dynamic experiments; furthermore, it is perhaps to be expected that measurement of a quantity that is deliberately close to zero has poor relative accuracy. However, overall it can be seen that the model fits the data well, and seems to capture the threshold base amplitude between isolated resonance and unconditional resonance.

### 5.3. Free responses with high frequency excitation

In these tests, the aim was to experimentally reproduce the behaviour discussed in Section 4, where a high frequency excitation broke the frictional locking effect. The base was set to a sinusoidal motion at a frequency significantly above resonance, and then the system was manually disturbed, first in a downward direction then in an upward direction, and the time series was measured.

Figures 13–15 show the results of these experiments in terms of relative velocity in parts (a) and (b) and relative displacement in parts (c) and (d) for a base frequency of 5 Hz, and base amplitudes 0.5 mm, 1.0 mm and 1.5 mm respectively. In the displacement plots (c) and (d), the red dotted line shows the raw data captured by the laser displacement sensors. To remove the direct effect of high frequency excitation from this signal, an FFT was taken of the entire time signal, and Fourier components at frequencies above 4 Hz were removed. The steady state component was also removed. An inverse FFT was then performed to give the time signal shown as the blue solid line in Figs. 13 to 15.

Finally, the black dashed line in these figures shows the results of a time simulation using the equivalent viscously damped system given in Eq. (23). The parameter values used were as given in Table 1, with the exception that $k_1$ was set to 28.3 N m$^{-1}$ to improve the fit of the results. Such variation in this parameter is not unexpected due to the reasons given in Section 5.2. This

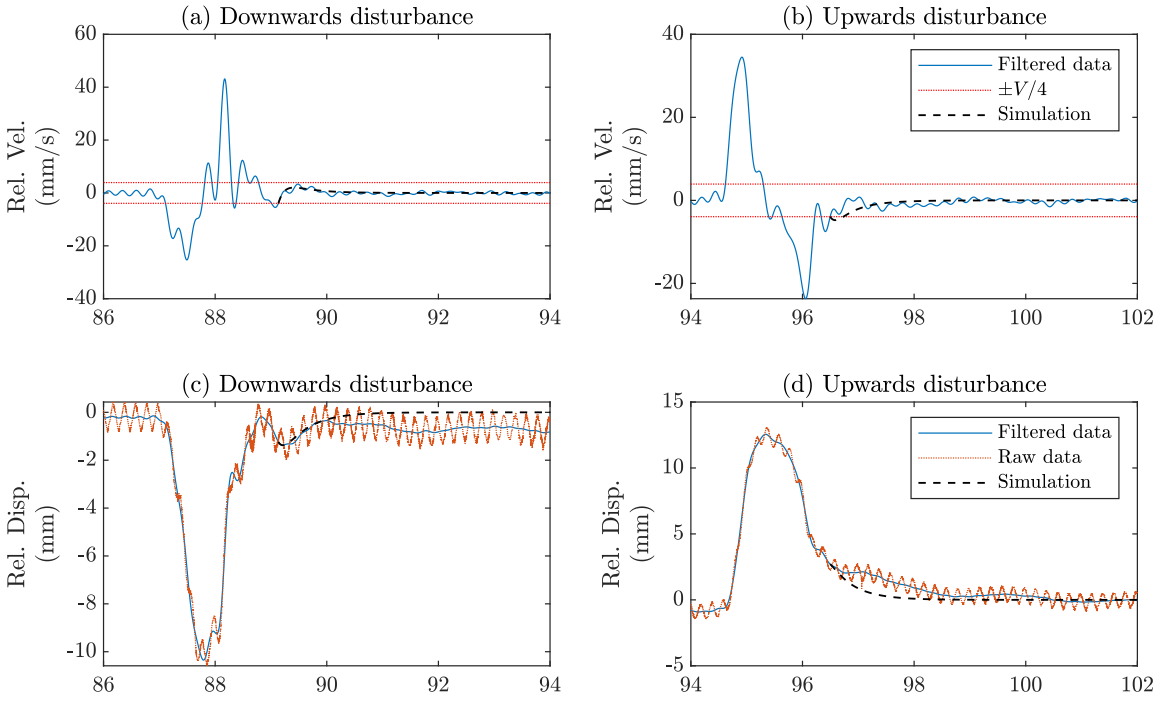


**Fig. 13.** Decaying response of system with sinusoidal base excitation at frequency 5 Hz, amplitude 0.5 mm.

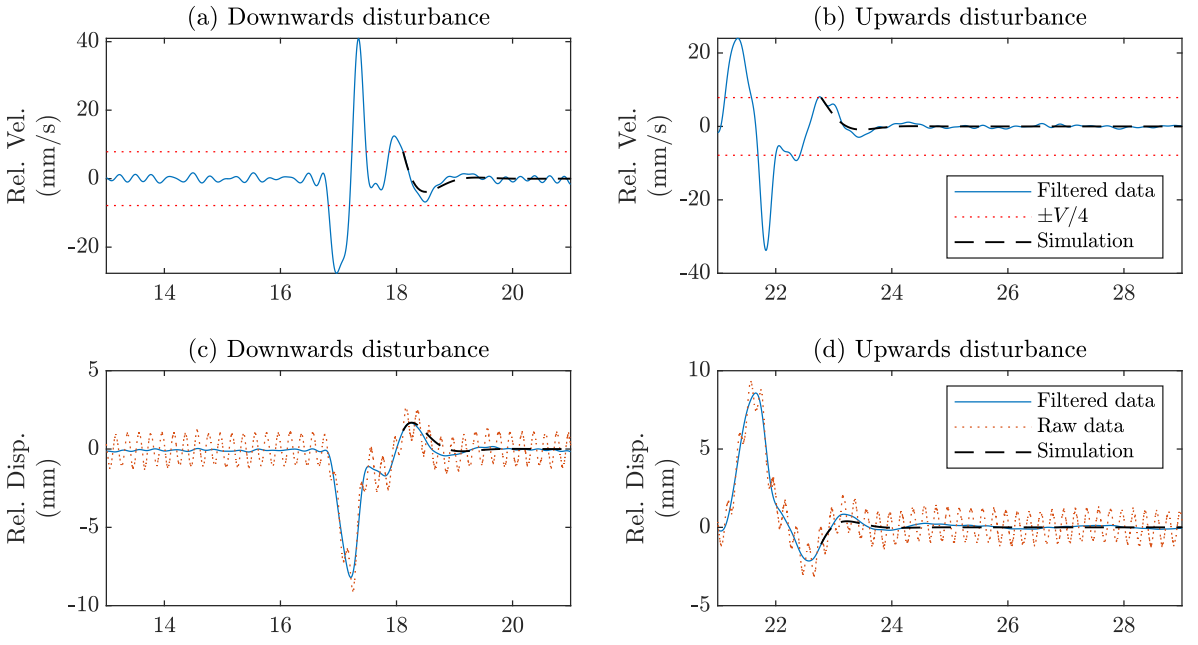


**Fig. 14.** Decaying response of system with sinusoidal base excitation at frequency 5 Hz, amplitude 1.0 mm.

time simulation is started at the time when the velocity falls below $V/4$ for the final time following the disturbance, when the assumption $\bar{v} \ll V$ can be considered valid. The initial conditions are the relative velocity and relative displacement interpolated from the filtered experimental data at this time.

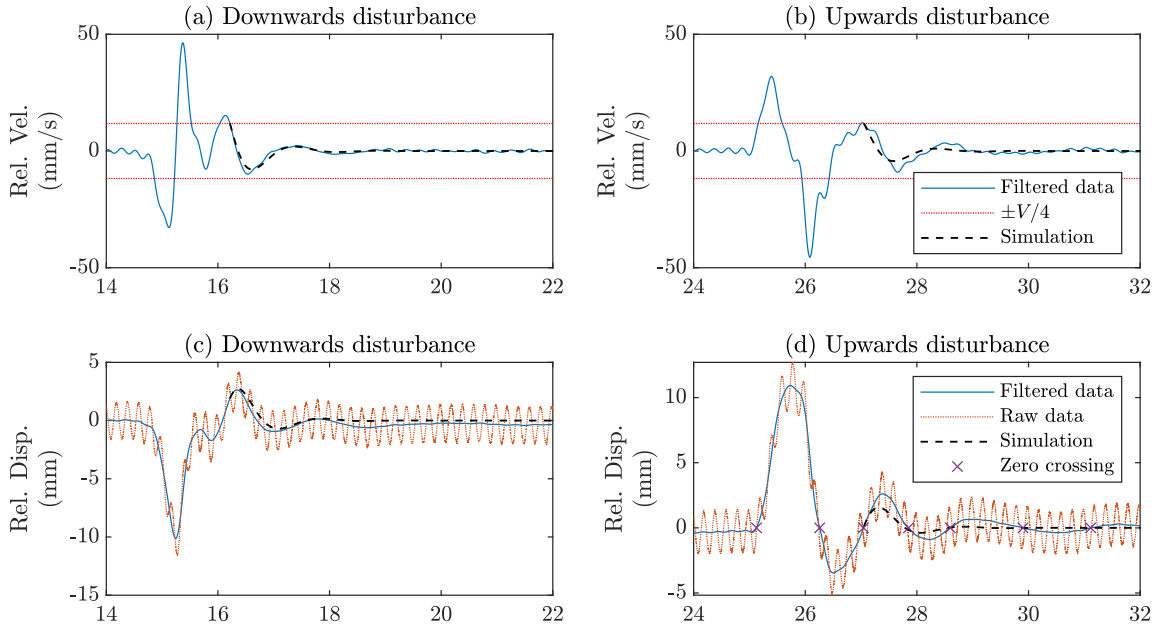


**Fig. 15.** Decaying response of system with sinusoidal base excitation at frequency 5 Hz, amplitude 1.5 mm.

These results show good qualitative agreement with the predictions of Section 4; during the disturbance and for a while afterwards where the underlying amplitude is still high, there is very little difference between the three cases. However, as the amplitude falls and the damping effect becomes active, the prediction that the equivalent damping falls with increased base amplitude is seen. In Fig. 13, there is almost no oscillation of the filtered signal at low amplitude, whereas Figs. 14 and 15 show some decaying oscillations, with Fig. 15 showing the lowest rate of decay.

The quantitative match to the equivalently viscous damped system given by Eq. (23) varies between the cases. In Fig. 13, the match is poor. However, an equivalent damping ratio for system (23) can be defined as

$$\bar{\zeta} = \frac{\bar{c}}{2\sqrt{k_1 m}}\,, \tag{24}$$

and this shows that the chosen parameters give $\bar{\zeta} = 1.29$ in this case, predicting an overdamped response at low amplitude and explaining the lack of decaying oscillations.

For the amplitudes of 1.0 mm and 1.5 mm, the predicted equivalent damping ratios are $\bar{\zeta} = 0.644$ and $\bar{\zeta} = 0.429$ respectively, so the rapidly decaying oscillations observed are the expected behaviour. Comparing the simulation time signal to the filtered data, an approximate match with the simulation can be seen, seemingly predicting higher damping than the experiment.

Figure 15 does allow a crude estimate of the low amplitude frequencies of the isolator and payload system, and thus how close to a 'zero frequency' device has been achieved. The zero crossings of the filtered displacement data are indicated in Fig. 15 (d), and these show that the periods for the first two complete cycles following the disturbance are 1.59 s and 2.05 s, or in terms of frequency 0.63 Hz and 0.49 Hz respectively. Of course these frequencies are very approximate and will be influenced by the high viscous damping caused by the higher frequency oscillations combined with the friction in the device.

### *5.4. Non sinusoidal response.*

Figures 16 (a-c) show the absolute acceleration time signals of the base and mass in a steady state. It is notable that the mass acceleration is not sinusoidal but closer to a square wave signal. This suggests that the friction force is the dominant force transmitted to the payload, because the friction force also acts like a square wave with amplitude $f_0$. It is also interesting that the absolute payload motion is almost the same in each case, despite the different base amplitudes. At base amplitude 0.5 mm, there is not much isolation of the mass in compared to the base. However, because the response amplitude remains constant, the relative isolation performance increases with increasing base amplitude. It is clear that for this type of stiffness device, absolute transmissibility is a poor way of characterizing the isolation behaviour because in the isolation region the response is approximately constant regardless of base amplitude. Note that in Fig. 16(c) an impact occurs in the base motion on each cycle, but this does not appear to have a general effect on the response.

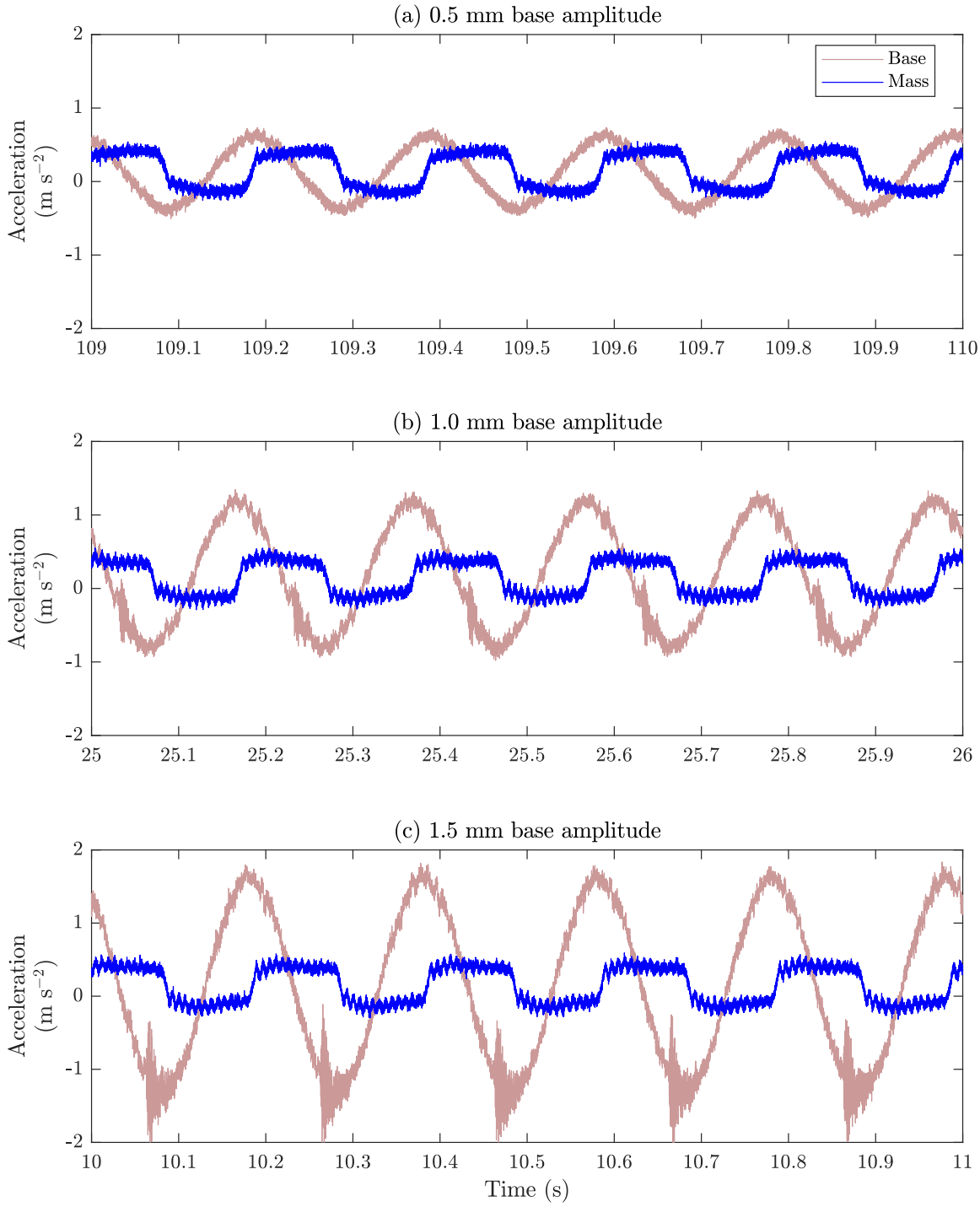


**Fig. 16.** Steady state acceleration responses at base frequency 5 Hz and amplitudes as shown.

## 6. Conclusions

The work described in this paper has shown experimentally that when a nonlinear QZS approaches the limit of zero stiffness, the true nature of the damping in the device has profound effects upon its resonant characteristics and isolation performance. When friction is present, as will typically be the case in any mechanism with joints or other linkages, it causes locked behaviour at low frequency and amplitude. Furthermore, it can cause branches of resonance to become isolated from the non-resonant response. This

behaviour is often desirable if an unbounded resonance needs to be avoided. Another effect is that when friction dominates, the roll-off in absolute response amplitude is reduced, and can become entirely dominated by forces transmitted through friction, with the base amplitude having little effect on the response amplitude. Finally, it was seen that if high frequency excitation is present, the frictional term can act similarly to a viscous damper on the low frequency dynamics of the QZS device, so long as the velocity due to low frequency motion does not exceed the velocity amplitude imparted by the response to high frequency excitation. This final phenomenon allows closer observation of the near-zero frequency dynamics of the isolator, but also raises some intriguing questions as to how high frequency motion in multi-modal structures may cause frictional interfaces to impart a viscous-like effect on lower modes.

## CRediT authorship contribution statement

**A.D. Shaw:** Conceptualization, Data curation, Formal analysis, Investigation, Methodology, Software, Writing – original draft. **G. Gatti:** Conceptualization, Validation, Writing – review & editing. **P.J.P. Gonçalves:** Conceptualization, Validation, Writing – review & editing. **B. Tang:** Conceptualization, Validation, Writing – review & editing. **M.J. Brennan:** Conceptualization, Validation, Writing – review & editing.

## Declaration of competing interest

The authors declare that there are no competing interests.

## Data availability

Data used in this work may be found at https://doi.org/10.5281/zenodo.10340200.

## Acknowledgements

This work was supported by the Royal Academy of Engineering, United Kingdom under the Distinguished Visiting Fellowships - Round 6, and also by EPSRC, United Kingdom grant EP/R006768/1 'Digital twins for improved dynamic design'. Data used in this work may be found at https://doi.org/10.5281/zenodo.10340200.

## References

[1] P. Alabuzhev, Vibration Protection and Measuring Systems with Quasi-Zero Stiffness, CRC Press, 1989.
[2] L. Virgin, S. Santillan, R. Plaut, Vibration isolation using extreme geometric nonlinearity, J. Sound Vib. 315 (3) (2008) 721–731.
[3] W. Robertson, M. Kidner, B. Cazzolato, A. Zander, Theoretical design parameters for a quasi-zero stiffness magnetic spring for vibration isolation, J. Sound Vib. 1–2 (2009) 88–103.
[4] B. Yan, N. Yu, C. Wu, A state-of-the-art review on low-frequency nonlinear vibration isolation with electromagnetic mechanisms, Appl. Math. Mech. 43 (7) (2022) 1045–1062.
[5] Y. Zheng, W. Shangguan, X. Liu, Modeling of a quasi-zero static stiffness mount fabricated with tpu materials using fractional derivative model, Mech. Syst. Signal Process. 177 (2022) 109258.
[6] S. Dalela, B. P.S., D. Jena, M. Leblouba, A tunable metamaterial using a single beam element with quasi-zero-stiffness characteristics for low-frequency vibration isolation, J. Vib. Control 10775463231198892.
[7] W. Liu, L. Wu, J. Sun, J. Zhou, Origami-inspired quasi-zero stiffness metamaterials for low-frequency multi-direction vibration isolation, Appl. Phys. Lett. 123 (8) (2023) 084102.
[8] C. Yu, Q. Jiang, Q. Fu, K. Yu, J. Zhang, N. Zhang, The X-shaped structure with nonlinear positive stiffness compensation for low-frequency vibration isolation, Int. J. Mech. Sci. 259 (2023) 108598.
[9] S. Zhou, P. Xu, B. Hou, Z. Ren, Dynamic characteristics analysis of bilayer bio-inspired X-shaped vibration isolation structure, Int. J. Non-Linear Mech. 154 (2023) 104447.
[10] B. Ding, X. Li, S. Chen, Y. Li, Modular quasi-zero-stiffness isolator based on compliant constant-force mechanisms for low-frequency vibration isolation, J. Vib. Control 10775463231188160.
[11] H. Han, L. Tang, J. Wu, S. Sun, P. Yin, D. Cao, Origami-inspired isolators with quasi-zero stiffness for coupled axial-torsional vibration, Aerosp. Sci. Technol. 140 (2023) 108438.
[12] K. Ye, J. Ji, R. Fitch, Further investigation and experimental study of an origami structure-based quasi-zero-stiffness vibration isolator, Int. J. Non-Linear Mech. 157 (2023) 104554.
[13] S. Liu, G. Peng, Z. Li, W. Li, L. Sun, Low-frequency vibration isolation via an elastic origami-inspired structure, Int. J. Mech. Sci. 260 (2023) 108622.
[14] I. Kovacic, M. Brennan, T. Waters, A study of a nonlinear vibration isolator with a quasi-zero stiffness characteristic, J. Sound Vib. 315 (3) (2008) 700–711.
[15] A. Vakakis, O. Gendelman, L. Bergman, D. McFarland, G. Kerschen, Y. Lee, Nonlinear Targeted Energy Transfer in Mechanical and Structural Systems, vol. 156, Springer Science & Business Media, 2008.
[16] O. Gendelman, Y. Starosvetsky, M. Feldman, Attractors of harmonically forced linear oscillator with attached nonlinear energy sink I: description of response regimes, Nonlinear Dynam. 51 (1) (2008) 31–46.
[17] Y. Starosvetsky, O. Gendelman, Vibration absorption in systems with a nonlinear energy sink: nonlinear damping, J. Sound Vib. 324 (3–5) (2009) 916–939.
[18] J. Zang, T. Yuan, Z. Lu, Y. Zhang, H. Ding, L. Chen, A lever-type nonlinear energy sink, J. Sound Vib. 437 (2018) 119–134.
[19] L. Zhao, H. Zou, K. Wei, S. Zhou, G. Meng, W. Zhang, Mechanical intelligent energy harvesting: From methodology to applications, Adv. Energy Mater. 13 (29) (2023) 2300557.
[20] M. Li, X. Li, C. Gan, J. Zeng, L. Zhao, H. Ding, K. Wei, H. Zou, Human motion energy harvesting backpack using quasi-zero stiffness mechanism, Energy Convers. Manage. 288 (2023) 117158.
[21] G. Yan, J. Lu, W. Qi, T. Zhao, H. Yan, L. Zhao, Z. Wu, W. Zhang, Tetrahedron structure with nonlinear stiffness and inertia modulation for enhanced low frequency vibration isolation, J. Sound Vib. 564 (2023) 117897.

[22] Z. Li, K. Wang, T. Chen, L. Cheng, D. Xu, J. Zhou, Temperature controlled quasi-zero-stiffness metamaterial beam for broad-range low-frequency band tuning, Int. J. Mech. Sci. 259 (2023) 108593.
[23] T. Liu, A. Li, H. Zhang, Quasi-zero stiffness interval optimization design and dynamics analysis of a new bi-directional horizontal isolation system, Mech. Syst. Signal Process. 206 (2024) 110852.
[24] X. Huang, X. Liu, J. Sun, Z. Zhang, H. Hua, Effect of the system imperfections on the dynamic response of a high-static-low-dynamic stiffness vibration isolator, Nonlinear Dynam. (2014) 1–11.
[25] X. Huang, X. Liu, H. Hua, Effects of stiffness and load imperfection on the isolation performance of a high-static-low-dynamic-stiffness non-linear isolator under base displacement excitation, Int. J. Non-Linear Mech. 65 (2014) 32–43.
[26] A. Shaw, S. Neild, M. Friswell, Relieving the effect of static load errors in nonlinear vibration isolation mounts through stiffness asymmetries, J. Sound Vib. 339 (2015) 84–98.
[27] K. Ye, J. Ji, T. Brown, Design of a quasi-zero stiffness isolation system for supporting different loads, J. Sound Vib. 471 (2020) 115198.
[28] G. Yan, Z. Wu, X. Wei, S. Wang, H. Zou, L. Zhao, W. Qi, W. Zhang, Nonlinear compensation method for quasi-zero stiffness vibration isolation, J. Sound Vib. 523 (2022) 116743.
[29] J. Lu, G. Yan, W. Qi, H. Yan, J. Shi, A. Chen, W. Zhang, Load-adaptive quasi-zero stiffness vibration isolation via dual electromagnetic stiffness regulation, J. Sound Vib. 567 (2023) 118059.
[30] T. Chen, Y. Zheng, L. Song, X. Gao, G. Wang, Study on a quasi-zero-stiffness isolator for variable mass load, Appl. Math. Model. 123 (2023) 447–463.
[31] W. Qi, G. Yan, J. Lu, F. Liu, T. Zhao, H. Yan, W. Zhang, Local gravity control method for solving load-mismatch issue in isolators, Int. J. Mech. Sci. 265 (2024) 108891.
[32] K. Xu, Y. Zhang, Y. Zhu, J. Zang, L. Chen, Dynamics analysis of active variable stiffness vibration isolator for whole-spacecraft systems based on nonlinear output frequency response functions, Acta Mech. Solida Sin. 33 (2020) 731–743.
[33] L. Liu, Y. Chai, Z. Guo, M. Li, A novel isolation system with enhanced QZS properties for supporting multiple loads, Aerosp. Sci. Technol. 143 (2023) 108719.
[34] X. Hu, C. Zhou, Dynamic analysis and experiment of Quasi-zero-stiffness system with nonlinear hysteretic damping, Nonlinear Dynam. 107 (3) (2022) 2153–2175.
[35] X. Hu, C. Zhou, The effect of various damping on the isolation performance of quasi-zero-stiffness system, Mech. Syst. Signal Process. 171 (2022) 108944.
[36] B. Ravindra, A. Mallik, Hard Duffing-type vibration isolator with combined Coulomb and viscous damping, Int. J. Non-Linear Mech. 28 (4) (1993) 427–440.
[37] A. Shaw, G. Gatti, P. Gonçalves, B. Tang, M. Brennan, Design and test of an adjustable quasi-zero stiffness device and its use to suspend masses on a multi-modal structure, Mech. Syst. Signal Process. 152 (2021) 107354.
[38] G. Gatti, A. Shaw, P. Gonçalves, M. Brennan, On the detailed design of a quasi-zero stiffness device to assist in the realisation of a translational Lanchester damper, Mech. Syst. Signal Process. 164 (2022) 108258.
[39] J. Meriam, L. Kraige, J. Bolton, Engineering Mechanics: Statics, Wiley, 2020.
[40] A. Shaw, S. Neild, D. Wagg, Dynamic analysis of high static low dynamic stiffness vibration isolation mounts, J. Sound Vib. 332 (6) (2013) 1437–1455.
[41] A. Carrella, M. Brennan, T. Waters, V. Lopes Jr., Force and displacement transmissibility of a nonlinear isolator with high-static-low-dynamic-stiffness, Int. J. Mech. Sci. 55 (1) (2012) 22–29.